Characterization of the Cloud-Topped Boundary Layer at the Synoptic Scale Using AVHRR Observations during the SEMAPHORE Experiment

A. MATHIEU

Centre d'etude des Environnements Terrestre et Planétaires/IPSL/CNRS, Vélizy, France

G. SÈZE AND A. LAHELLEC

Laboratoire de Météorologie Dynamique/IPSL/CNRS, Université P. M. Carie, Paris, France

C. GUERIN AND A. WEILL

Centre d'étude des Environnements Terrestre et Planétaires/IPSL/CNRS, Vélizy, France

(Manuscript received 29 March 2002, in final form 9 June 2003)

ABSTRACT

Satellite platforms *NOAA-11* and *-12* Advanced Very High Resolution Radiometer (AVHRR) data are used during the daytime to study large sheets of stratocumulus over the North Atlantic Ocean. The application concerns an anticyclonic period of the Structure des Echanges Mer–Atmosphère, Propriétés des Hétérogénéités Océaniques: Recherché Expérimentale (SEMAPHORE) campaign (10–17 November 1993). In the region of interest, the satellite images are recorded under large solar zenith angles. Extending the SEMAPHORE area, a region of about 3000×3000 km^2 is studied to characterize the atmospheric boundary layer. A statistical cloud classification method is applied to discriminate for low-level and optically thick clouds. For AVHRR pixels covered with thick clouds, brightness temperatures are used to evaluate the boundary layer cloud-top temperature (CTT). The objective is to obtain accurate CTT maps for evaluation of a global model. In this application, the full-resolution fields are reduced to match model grid size. An estimate of overall temperature uncertainty associated with each grid point is also derived, which incorporates subgrid variability of the fields and quality of the temperature retrieval. Results are compared with the SEMAPHORE campaign measurements. A comparison with ''DX'' products obtained with the same dataset, but at lower resolution, is also presented. The authors claim that such instantaneous CTT maps could be as intensively used as classical SST maps, and both could be efficiently complemented with gridpoint error-bar maps. They may be used for multiple applications: (i) to provide a means to improve numerical weather prediction and climatological reanalyses, (ii) to represent a boundary layer global characterization to analyze the synoptic situation of field experiments, and (iii) to allow validation and to test development of large-scale and mesoscale models.

1. Introduction

It is well established that boundary layer clouds play an important role in climate and climate change. Because their temperature is close to that of surface values, they do not significantly modify radiation losses to space; in comparison with oceanic surfaces, however, the large cloud albedo strongly lowers the impact of solar visible flux on the surface energy budget. Satellite observations have confirmed the frequent occurrence of stratocumulus cloud (Sc) over large oceanic areas, in particular over eastern subtropical regions of ocean basins (Harrison et al. 1991).

The representation of boundary layer (BL) characteristics is an important feature of global circulation models, but current versions are still unsatisfactory. For instance, the vertical transport of water from the surface is not realistic enough in models (e.g., Lock et al. 2000). The reason for these deficiencies, despite 30 years of experimental and theoretical studies, may be found in the complexity of mesoscale secondary flows within the boundary layer. These motions are the results of strongly coupled physical phenomena (Stull 1997). For all of these reasons, BL cloud studies are still an active part of field experiments and modeling efforts. As compared with global model validation requirements, field experiments are documenting the boundary layer on a very short spatial range. Nowadays, a current practice is to build case studies for comparison with single-column models [as in Global Energy and Water Cycle Experiment (GEWEX) projects]. Our objectives are to examine

Corresponding author address: Anne Mathieu, Laboratoire de Météorologie Dynamique/IPSL/CNRS, Ecole Polytechnique, 91128 Palaiseau Cedex, France.
E-mail: amathieu@lmd.polytechnique.fr

the possibility of describing the boundary layer on a broader scale from satellite observations, to allow for comparison with global models at a proper scale.

Characterization of the boundary layer from a satellite is not straightforward: even in regions of subsidence, BL clouds have varying texture and structure and may be hard to discriminate from the surface. Various authors have used satellite data to determine cloud fractions (e.g., Norris and Weaver 2001). Another important parameter is the cloud-top temperature (CTT). This parameter is linked with the height of the BL, which is well defined in regions of subsidence. In such regions, BL clouds are typically capped by an inversion layer, so that the cloud-top altitude is representative of BL height (Stull 1998). The BL height (BLH) is an important parameter for both observational and theoretical purposes because it represents a primary integral characteristic of the boundary layer, resulting from various multiscale coupled phenomena (e.g., Ciesielski et al. 2001). Minnis et al. (1992) and Betts et al. (1991) studied the monthly mean diurnal cycle of BL height during the First International Satellite Cloud Climatology Project (ISCCP) Regional Experiment (FIRE) experiment, making use of CTT. Bretherton and Pincus (1995) also attempted to use CTT to analyze cloud transitions during the Atlantic Stratocumulus Transition Experiment (ASTEX) experiment, but with no success.

Similar to the ASTEX campaign, the current study focuses on specific meteorological situations in which one is more concerned with local particularities and with their interpretation. A conversion from CTT to BLH as in Minnis et al. (1992) necessitates hypotheses on the thermodynamic profiles of the atmosphere. We preferred avoiding any extra hypothesis and aimed at delivering more direct information, that is, maps of CTT fields. It is shown in this paper that it is possible to document efficiently the boundary layer with low-level CTT maps and errors. This information, completed by a characterization of cloud structures, is of primary importance for comparison with models, because their spatial variations are signatures of physical processes. This has been demonstrated, for instance, in the study of transitions from Sc to trade wind cumuli along airmass drifts from ocean-upwelling regions to southwestward tropical regions (Krueger et al. 1995; de Roode and Duynkerke 1997).

The following application concerns the analysis of the boundary layer in the North Atlantic Ocean over a region of approximately 3000×3000 km^2, containing the SEMAPHORE[1] intensive zone of observations (IZO). The SEMAPHORE campaign (Eymard et al. 1996) has been one of many others dedicated to air–sea exchanges (Agee and Dowell 1974; Grossman 1982; Nicholls and LeMone 1980; Krueger et al. 1995; Bretherton and Pincus 1995). The field experiment took place in October–November of 1993 in the Azores region. An objective was to characterize BL clouds in the context of a stable anticyclonic situation in the region from 10 to 17 November 1993. During the period, extensive low-level cloud cover is observed. A fair diversity of cloud scenes can be seen, as on the Advanced Very High Resolution Radiometer (AVHRR) image (Fig. 1). Apart from the large sheets of cirrus in the north-northwest part, low-level clouds are seen over extended regions. A few benches of Sc clouds look uniform. Closed cells are seen around (32°N, 30°W); clouds streets are observed in the (36°N, 15°W) zone. Such a synoptic view offers a variety of BL states that a model should recover if its representation of the physics of the boundary layer is correct.

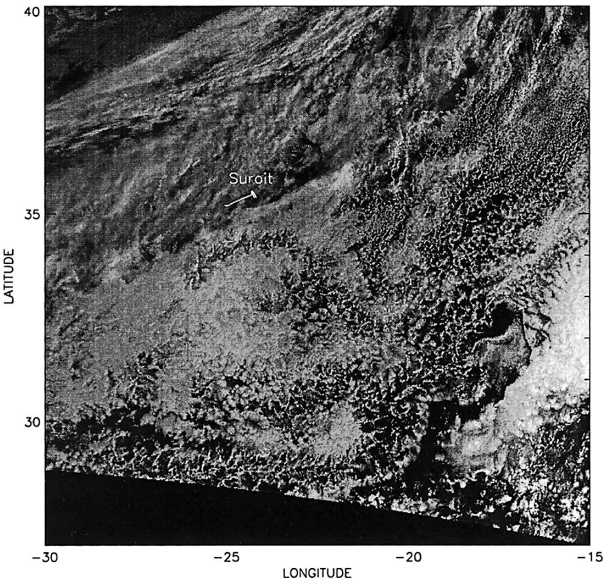

FIG. 1. Zoom from the AVHRR image at 0847 UTC 15 Nov 1993.

In this article, we propose a method to quantify the signature of these physical phenomena to allow comparison with model predictions. The first step consists of the identification of BL clouds from their optical characteristics (section 2). The selection of unambiguously cloudy pixels allows one to derive CTT maps (section 3). The method provides two-dimensional error-bar maps that should be useful for model evaluation, improvement, and assimilation. The results are compared with the AVHRR-DX products of the ISCCP (section 4a). We make use of the BL documentation built up from the campaign to evaluate the precision of our results (section 4b).

2. Cloud-scene classification

The visible and infrared channels of the satellite radiometers allow us to observe BL liquid water clouds. The visible channel provides indirect information on cloud thickness, and the brightness temperature provide

[1] Structure des Echanges Mer-Atmosphère, Propriétés des Hétérogénéités Océaniques: Recherche Expérimentale.

information on cloud altitude. We use this information to detect and discriminate among clouds. To select BL clouds, one requires (i) good cirrus detection and rejection, which can be difficult for thin clouds; (ii) discrimination among low-level cloud types; and (iii) identification of partially covered pixels, especially in broken cloud regions.

The AVHRR data are recorded during the winter season, close to sunrise or sunset, with solar zenith angles typically over 63°. This value is recognized as a limit for application of the plane-parallel model of clouds (Loeb and Coakley 1998). This tends to complicate the characterization of clouds, especially when in broken decks, as will be discussed in section 3. To address these points, we chose a statistical cloud classification method. Using a whole set of cloud scenes, the method allows one to capture the different characteristics of the clouds as they are observed with the dataset.

a. The cloud classification method

The cloud classification method is based on the dynamic cluster method (DCM; Sèze and Desbois 1987; Desbois et al. 1982). DCM has been developed mainly for the exploitation of visible and infrared radiance fields observed by Meteosat (Sèze and Pawlowska 2001). Application to AVHRR data has already been performed by Giraud (1994) for cirrus studies. For a given region and period, and given a set of n parameters at pixel scale, the histogram in the n-dimensional (nD) space of parameters is built up. The histogram is partitioned in classes representative of surface and cloud types, each defined by its center of mass and variance in the parametric space. The algorithm, an iterative process starting from randomly initialized classes, does not require any knowledge of the classes, a priori, but requires a maximal number of them (chosen as equal to 40 in this case). However, the solution is not unique. Several initial random draws are tried. The retained solution is the one having well-separated and compact classes. Then, each pixel in each individual image is projected in the nD space and is assigned to the nearest class (Euclidian distance in the nD space of parameters). The labeling of classes with a cloud-type name is performed visually using the center-of-mass positions of the classes.

For this analysis, four spectral parameters are available from National Oceanic and Atmospheric Administration *NOAA-11* and *-12* AVHRR satellite data: R1 and R2 reflectances in the visible (0.6 and 0.9 μm), and, for the two IR bands T4 and T5 (10.8 and 12 μm), brightness temperatures. For reflectance, channel 2 is taken into account because it is less sensitive to molecular scattering effects and aerosols (Saunders and Kriebel 1986). For brightness temperature, channel 5 (T5) is used because it is more sensitive to thin cirrus.

In addition to R2 and T5, we also use their associated structural parameters—that is, the standard deviations computed from the 3×3 values centered on the pixel (3×3 rms). The use of local variability of the visible and infrared radiance allows one to have a good separation between completely clear sky pixels from ones partially covered by either low broken clouds or thin higher clouds.

b. Application and results

DCM is applied to the 15 AVHRR images provided during the studied period. Numerous tests have been preformed to check for the sensitivity to solar zenith angles of the retrieved classes, showing that the classification is not significantly affected when applying thresholds on the angles. DCM is applied to the 4D parameter distribution obtained from the pixels of the 15 AVHRR images without any restriction on solar zenith angles. Only oceanic pixels have been taken into account.

Among the 21 classes finally obtained, 9 can be identified as low-level cloud classes (cumulus to stratus clouds) and 8 characterize the presence of high-level clouds (cirrus and cumulonimbus). Classes labeled *multi* are found mainly at the edge of cirrus sheets, indicating thin cirrus over lower clouds. The period does not show any intermediate-level clouds.

The mean reflectance and brightness temperature values of each class are given in Fig. 2a. The y axis represents brightness temperature, and reflectance is along the x axis. The magnitude of the two bars centered on each mass center gives the visible and infrared 3×3 rms structure parameters. The shape in the reflectance/brightness temperature space corresponds to cirrus with varying emissivity and to low-level cloud cover with varying coverage inside the pixel (Platt 1983; Sèze and Rossow 1991). Starting from the darkest and warmest clusters, the orange branch shows the progression from clear sky to small cumulus and thick low cloud decks (green). The turquoise follows the progression from thin cirrus to high thick clouds. For clouds with variable optical thickness or multilayered clouds, the visible and infrared luminance vary alike; thus, their discrimination is difficult. The two spatial variances of the luminance allow the distinction. For example, the sea surface gives very low 3×3 rms; thick Sc clouds exhibit the same low IR 3×3 rms but their varying thickness results in a higher visible variance. For identification of cirrus, IR variance is more important than in the visible, and partially covered pixels will be characterized by both visible (VIS) and IR high variance.

Figure 3a shows the results of the classification method applied on 15 November data. Among low-level clouds, the classes indicated by green colors (7, 8, 9, 11, and 12) exhibit more spatial homogeneity in the IR. They typically appear as large sheets of Sc. Classes in brown and orange colors indicate Sc also, but nonuniform, some of them being characterized by high IR variance (3, 5, 6, and 13). They correspond to either thin

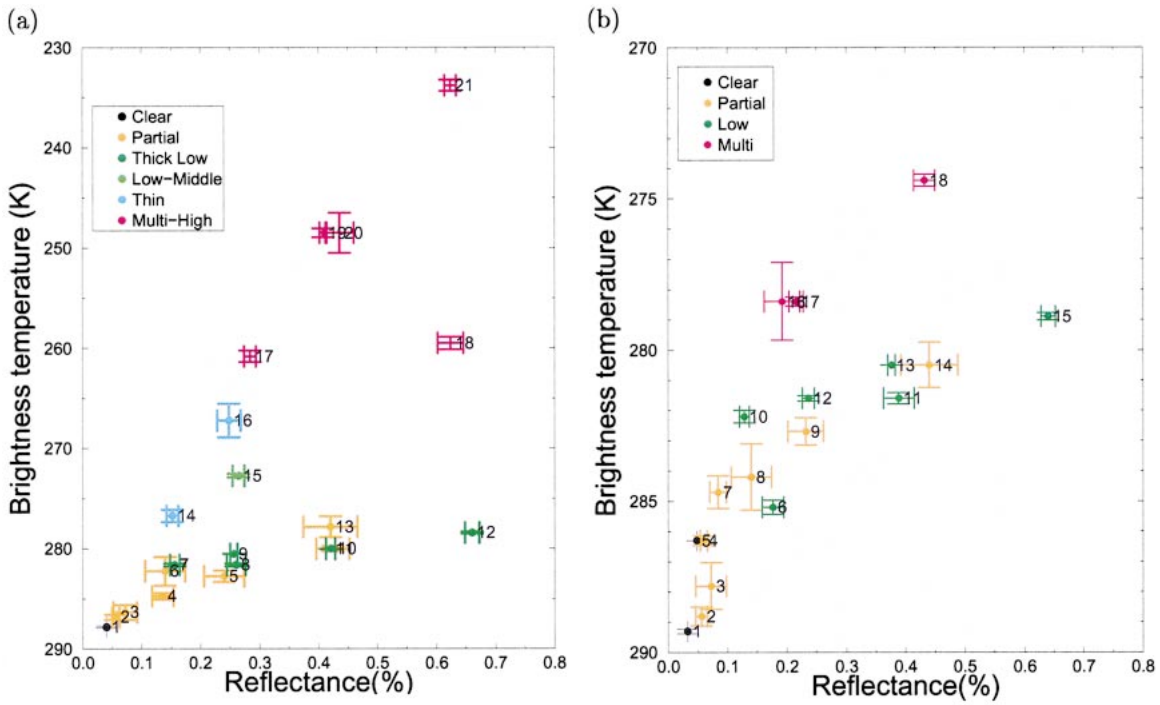

FIG. 2. Mean reflectance (*x* axis) and brightness temperature values (*y* axis) of each class (a) for all pixels and (b) after masking of the high clouds. The magnitudes of the two bars centered on each mass center give the visible and infrared 3 × 3 rms structure parameter. The cirrus are in turquoise (from thin to high thick clouds). The thick low-level cloud decks are in green. The orange branch shows the progression from clear sky to small cumulus.

Sc or fractional low-level clouds, as revealed by a statistical analysis of neighboring classes. They are mostly present in regions of organized structures. The 0847 UTC view shows that the region is mainly covered with low clouds, except in the northern part, where an extended sheet of cirrus is present. Two extended homogeneous Sc sheets are seen in green (east and southwest of the image); the rest is mostly covered with broken clouds.

The classification method has been applied to the same set of images after masking high-level clouds—classes labeled 16–21. This reprocessing was done to check for the detection of high clouds and to obtain more refined discrimination among low-level clouds. It

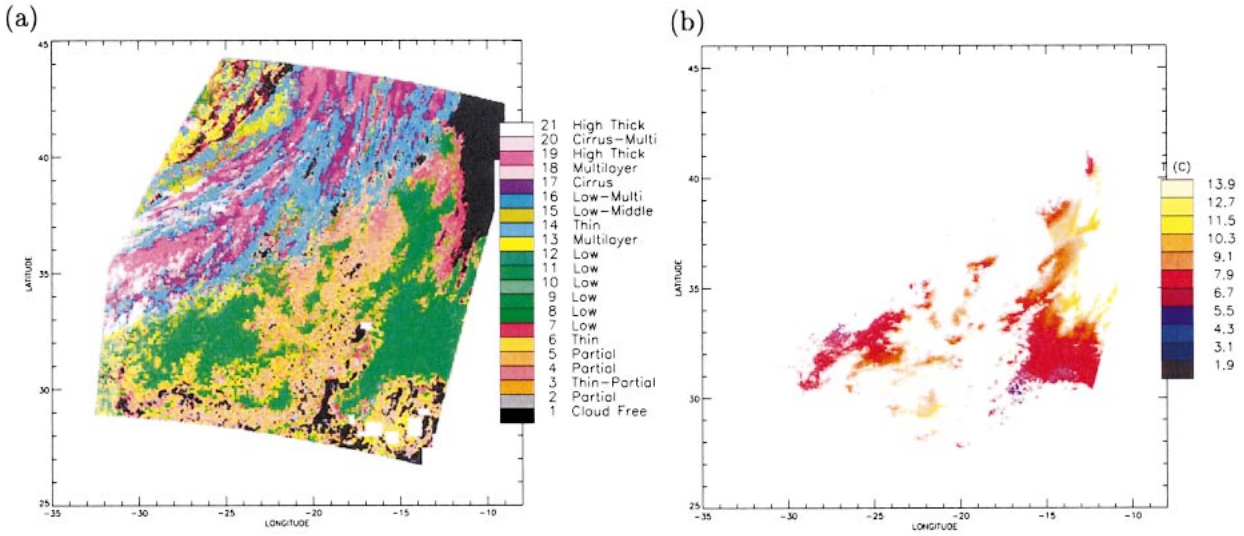

FIG. 3. (a) Result of the cloud classification at 0847 UTC 15 Nov and (b) boundary layer CTT at pixel resolution.

gives rise to a new set of 18 classes, for which an analogous color coding has been defined. Figure 2b shows the resulting VIS/IR distribution of classes. A statistical comparison between the two classifications shows that discrimination between cloud types is robust: one gets mostly the same partition between broken low-level clouds. For instance, we now have classes 2, 3, 4, 7, 8, and 14 as brown and orange, and homogeneous clouds classes (11, 12, 13, and 15) are in green. Some precision has been gained on low-level cloud types, primarily due to new less-uniform classes (6, 9, and 10). Other classes are signaling the presence of thin cirrus (16, 17, and 18). They are principally situated on the border of regions already marked as high-level clouds. Such differences were causing intraclass dispersion in the first classification, whereas they now are gathered into distinct classes.

In summary, the second classification is better at discriminating among low-level cloud classes and, considering the better detection of thin cirrus regions, allows one to improve rejection of ambiguous information.

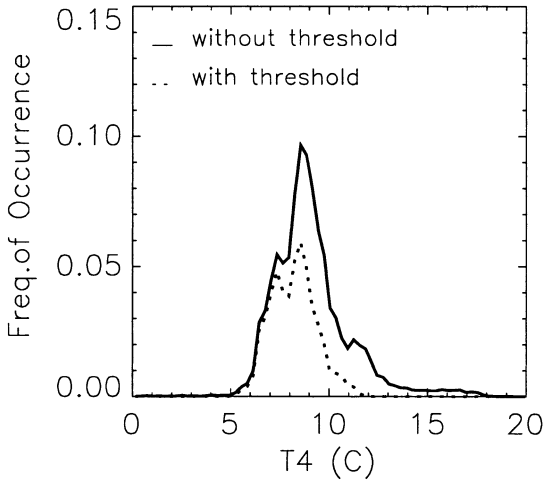

FIG. 4. Channel-4 brightness temperature distribution for pixels of classes 11, 12, and 13 at 0847 UTC 15 Nov (solid line). Dashed line denotes pixel distribution with threshold on the visible ($R2 > 0.25$) and the split window ($T4 - T5 < 0.9$).

3. Retrieval of the cloud-top temperature

a. Retrieval at pixel resolution

Using the mean features of the resulting classes of the previous analysis, we select particular cloud scenes allowing for a direct derivation of CTT from brightness temperature. Another approach commonly used is a physical bispectral method applied to all clouds (Rossow et al. 1985; Minnis et al. 1992). In such a method, the optical thickness of the cloud is evaluated from the delivered AVHRR bidirectional reflectance (R1). An effective infrared cloud emittance is estimated from this visible optical thickness, and the CTT is derived from the comparison between measured brightness temperatures of clouds and clear-sky scenes. In the current case, the large solar zenith angles render that problem more complex. Indeed, the usual procedure for retrieving the cloud optical thickness is based on the plane-parallel assumption, which has proven to be irrelevant as soon as zenith angles are large (Foot 1988; Loeb and Coakley 1998; Buriez et al. 2001). The problem is even enhanced for irregular cloud summit and broken cloud decks (Loeb et al. 1998). Faced with such difficulties, we adopted a more conservative approach. We select the most homogeneous clouds in the infrared and the most reflective among available cloud types and then assume blackbody emission in the 10–11-μm band. The band is in the atmospheric window, and so the absorption is at minimum. Therefore, we take the brightness temperature (T4) as the best estimate of CTT.

The visible and IR 3×3 variances provide information on cloud-deck homogeneity. Among the low-level cloud classes, full cloudy pixels are selected by the rejection of both high-rms and low-reflective classes. This process leads to keeping classes labeled 11, 12, 13, and 15. Class 15 is subsequently rejected as corresponding to high forward viewing angles (120°), which are close to specular reflection. Among the residual classes 11, 12, and 13, pixels in 11 and 13 have a reflectivity of approximately 40% and are considered optically thick enough. This value is justified by classical results of plane-parallel radiative transfer models and is analyzed in section 4a. Class 12 has a lower reflectivity, but, considering its occurrence in very homogeneous cloudy regions, the pixels of this class are kept if they are above a first threshold of 25% on their reflectance. This value may seem too low to characterize optically thick clouds, but again it may correspond to bumpy-topped clouds for which, at these large incidence angles, the apparent reflectance may be lowered by as much as 30% for large and oblique view angles (Loeb et al. 1998). These ambiguous pixels are kept before applying another cut, as described below.

Roozekrans and Prangsma (1986) and Minnis et al. (1998) have shown that $T4 - T5$ (split window) can be used to discriminate between optically thick low-level clouds and totally covered pixels. This quantity is influenced both by SST and the atmospheric absorption. The same threshold $T4 - T5 < 0.9$ K has been applied on a pragmatic approach, with a higher value keeping pixels belonging to ambiguous regions.

Figure 4 shows the effect of the two applied thresholds on the T4 distribution for one AVHRR image, as representative of the set of data. Some of the warmest pixels have been eliminated, as expected, because they may correspond to clouds thin enough to let SST contribute to the brightness temperature of the pixel. A more detailed analysis shows that pixels in class 13 are nearly all conserved, but only one-half of the pixels in classes 11 and 12, with a clear rejection of the warmest part of the histograms. No general conclusion can be drawn

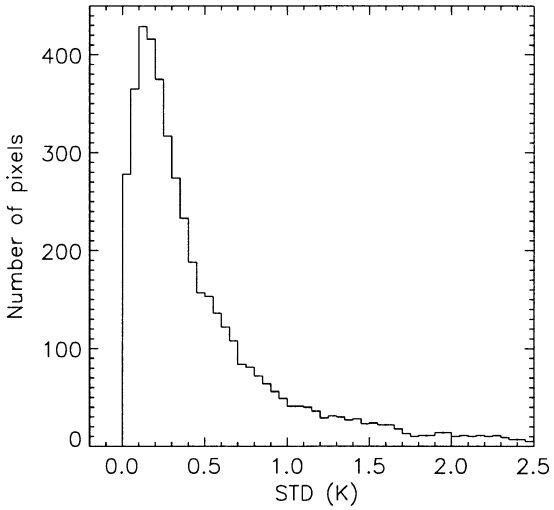

FIG. 5. Standard deviation of the CTT for a neighborhood of 10×10 pixels.

from the two retained values for R2 and the T4 − T5 threshold, because they are chosen for a particular treatment of both *NOAA-11* and *-12* radiometers under peculiar solar and oblique viewing angle conditions.

Figure 3b shows the resulting CTT for low-level clouds. It concerns the AVHRR data at 0847 UTC 15 November. Temperatures are varying between 6° and 11°C, with gradients of a few kelvin over a few hundred kilometers. One can observe a very good pixel-to-pixel coherence in the regions of homogeneous Sc decks. Over more broken clouds, only some isolated pixels provide a temperature, but they are generally in agreement with the neighboring compact zones. There remain some very isolated pixels with low temperature values that may result from undetected thin cirrus. These pixels are not eliminated even when restricting the thresholds; they represent a residue of the statistical treatment.

The overall strong pixel-to-pixel coherence is demonstrated by the histogram of Fig. 5. The figure shows the T4 dispersion of every selected pixel among their 10×10 neighbors approximately corresponding to a region of 30×30 km^2.

The previous maps are direct channel-4 brightness temperatures, without any correction for atmospheric absorption. To get an idea of absorption effects on the CTT maps, a classical SST correction algorithm is applied (Antoine et al. 1992). One mainly obtains a bias, smoothly increasing with viewing angle, corresponding to the thickening of the light path through the atmosphere: from 1 K at nadir to 2 K on edges (not shown). The resulting low gradients do not significantly affect the synoptic spatial variations of CTT fields.

b. *Determination of CTT at general circulation model grid resolution*

AVHRR pixels are gathered to obtain temperature retrieval at the resolution of our global model of reference: Action de Recherche Petite Echelle Grande Echelle (ARPEGE), 30×30 km^2 in the area of interest (Giordani and Planton 2000). Each grid cell gathers about 100 AVHRR pixels. The median of cloud pixel temperature is chosen to define the CTT of each grid point. This choice is motivated by several reasons. First, we want to avoid giving too strong a weight to aberrant pixel temperature that would have been misclassified by DCM. Thus, in case of overshooting, this tends also to increase moderately the gridpoint temperature, in comparison with taking the mean. The minimum number of cloudy pixels needed to determine a gridpoint temperature has been fixed to 10% of the maximum (~10 pixels here). This value ensures in particular that isolated pixels provide no information to the database.

Figure 6a shows the final-resolution CTT fields at 0847 UTC 15 November. One can verify that the full-resolution CTT gradients are conserved at the synoptic scale. Even broken cloud decks are documented, and aberrant pixels have disappeared. An improvement of the overall reliability is apparently reached.

To complement CTT fields, we document compound information on the subgrid variability, which we interpret as a precision on the fields for the following reasons. In some regions, BL cumuli gain enough energy to overshoot the mean inversion level. Overshooting is typically of a few tens of meters in the vertical direction and extends horizontally no more than a few hundred meters. They follow the geometric structure of the cloud decks over more extended regions. At 1-km resolution, they can result in detectable temperature variation from pixel to pixel. In addition, the selection of cloudy pixels may have included some optically inhomogeneous pixels, leading to an increased uncertainty on the retrieved temperature. Figure 5 shows a tail in the CTT distribution. There is no way to determine the reason why a given pixel contributes to the tail. We thus pragmatically consider that we obtain from pixels a sampled measure of CTT at the grid resolution, with an uncertainty given by the rms. Following the same view, the number of participating pixels in the gridpoint temperature definition is also accounted for. The definition of the error is taken as

$$\epsilon = \frac{\sigma\sqrt{N}}{\sqrt{n-1}}, \tag{1}$$

where N is the maximum number of pixels in a grid cell, n is the number of participating pixels, and σ is the pixel mean quadratic distance to the median temperature.

The error fields associated with the previous CTT map are shown in Fig. 6b. A high reliability for homogeneous cloud decks is obtained—a few tenths of kelvin—as compared with a few kelvin on broken clouds. These error fields should, in particular, be of primary importance to the assimilation procedure when minimizing weighted residual distance between forecast and mea-

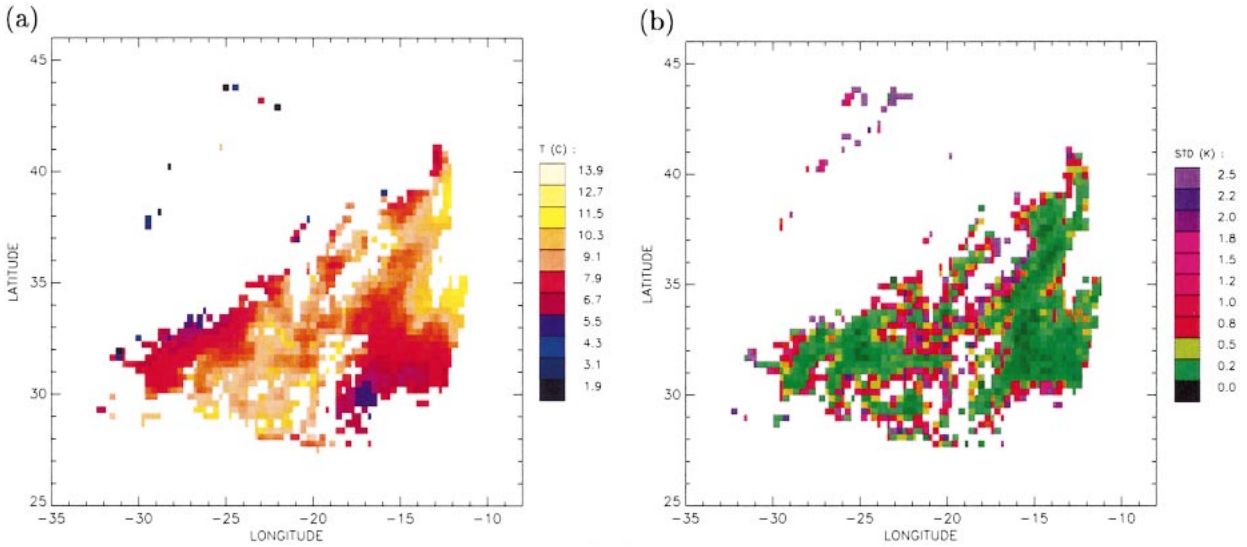

FIG. 6. (a) Boundary layer CTT at the 30 × 30 km² resolution at 0847 UTC 15 Nov and (b) associated error bars.

sured parameters. In the assimilation process, variance–covariance matrices are used to build ''structure functions'' related to a specific model. They are taken as constant on a given region for each type of parameter, when we obtain here a local determination, with a stronger weight applied to points with accurate CTT. This approach also allows one to keep documentation on important regions such as cell types of cloud decks. The retrieved CTT fields for the full period of our study were available online at the time of writing (http://www.cetp.ipsl.fr/mathieu/SEMAPHORE.html).

As already pointed out, in the absence of a reliable correction method for atmospheric absorption, a conservative way of using CTT maps relies on spatial gradients more than on absolute values. If one is focusing on a physical analysis of BL processes, synoptic variations are of primary importance as compared with absolute values of the parameters, provided SST fields are known elsewhere. Synoptic variation provides a means of studying the impact of mesoscale processes on the large scale and is most important for three-dimensional model evaluation. Compact CTT fields that allow for such gradient determination are found for large regions of 9 among the 15 available AVHRR images, with the 11 and 12 November cloud scenes being hardly usable. Such documentation of an important characteristic of the boundary layer, considered with its associated error-bar fields, could be useful for meteorological analyses and climatological reanalyses.

4. Evaluation of the quality of CTT maps

a. Comparison with ISCCP-DX database

As a global check of our CTT retrieval method, we made a comparison of our results with those available in the ISCCP-AVHRR-DX dataset (Rossow et al. 1996). In the DX method, the original AVHRR data (same as for this study) are first averaged to 4 km and then sampled to 30 km. To derive optical cloud properties, the algorithm applied at the pixel level is a two-stage process: first, cloudiness determination, and second, retrieval of cloud optical properties. The AVHRR-DX product is provided on a regular grid of 0.25°. To detect cloudy pixels, the algorithm is based on a threshold technique using clear-sky composite images obtained from the dataset itself. The approach used to derive cloud properties is a physical bispectral method (section 3a). The database gives access to cloud brightness temperature (with no correction), CTT (corrected for atmospheric absorption above cloud), and CTT corrected for small optical thickness. The latter parameter is available for solar zenith angles smaller than 78.5° only.

To separate cold clouds from warm clouds, we apply a threshold of 276 K on the DX brightness temperature (BT), instead of the 680-hPa pressure threshold used in the ISCCP dataset (Rossow et al. 1996). The warm-cloud BT compares well with our CTT maps. In the DX set, there is a larger abundance of pixels in regions of low broken clouds or in the neighborhood of cold clouds. These differences happen because the DCM identifies the ambiguous pixels that are partially cloudy or are covered by higher-level clouds. The small influence of the atmospheric absorption is verified by comparing the DX maps of BT and CTT. The correction is lower than 2 K for 90% of the points. This result is in agreement with the results of our estimation presented in section 3. Because of the 78.5° threshold on solar zenith angle, regions of useful information in the DX map of CTT obtained after correction for nonopaque clouds are limited. For those regions, comparison between temperature fields, corrected or not, shows differences often smaller than 2 K. Larger differences ap-

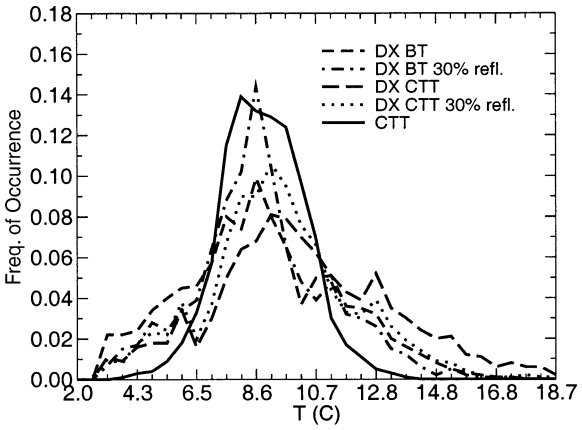

FIG. 7. Temperature distributions for the 10–17 Nov period from DX product compared with our CTT determination. Legend: see text.

pear again in regions of broken clouds or close to upper-level cloud systems. If a 30% threshold on reflectance is applied, the differences decrease. However, large differences appear in regions of sun glint, which are regions for which the retrieved cloud optical thickness is the most uncertain.

To perform a more precise comparison between the DX set and our CTT maps, the two resolutions have to be matched. The same algorithm that was previously used to build CTT maps at the GCM resolution is applied. In the current case, the resolution is 0.25° (about 8×8 pixels of the full-resolution grid). For the DX data, four types of map are built: 1) brightness temperature with a 276-K threshold (IR276), 2) same as type 1 with an added reflectance threshold of 30% (IR276 R30%), 3) CTT maps corrected for small optical thickness (T276), and 4) same as type 3 with an added reflectance threshold of 30% (T276 R30%).

The CTT distributions obtained with each set of maps are compared in Fig. 7: for DX curves, spreading toward colder temperature is observed for the BT curve, and spreading toward warmer temperature is observed for the CTT corrected for small optical thickness. Application of a 30% threshold on reflectance leads to a decrease of spreading. Peak and mean values are closed to our own CTT determination and range between 8 and 9 K. The standard deviation of our CTT maps is the smallest; the shape of the distribution is narrow in comparison with the other distributions. In comparison with the DX retrieval, our method eliminates some of the coldest or warmest pixels, the very ones that have been found to be ambiguous in our classification method.

In conclusion, the statistical classification gives access to more selective information than does a direct use of the DX product. However, if focusing on BL clouds, one can start with DX data and discriminate for low-level clouds with a threshold on CTT—or brightness temperature—and reflectance. In the case of difficult angle conditions as here, the two corrections proposed in the DX base may be used as an evaluation of uncertainty. As compared with our method, this procedure may keep regions that are partially covered with high clouds or very broken low clouds but should nevertheless provide useful information.

b. Validation using SEMAPHORE data

The main objectives of the SEMAPHORE experiment were to investigate the thermal and dynamic structures of the atmosphere and ocean in the presence of the Azores oceanic front. Ships, aircraft, and buoys were used to measure the atmospheric and oceanic properties around the front. Radiosondes where launched every 6 h from ships, and a tethered balloon (500 m) was periodically used for finer measurements, as was the 10-m mast of one ship. Aircraft measurements included radiation, turbulence and droplets spectra, and lidar observations.

For our objective of BL-top determination, we made use of the soundings from the oceanographic ship *Le Suroit* and of aircraft soundings. Soundings from two airplanes are recorded during favorable meteorological situations only, in the middle of the day, that is, never coincident with any of the two satellite passages. When we have to compare lagged measurements, grid points keeping the same characteristic cloud type between morning and afternoon images are selected. The soundings allow us to determine the existence and altitude of BL clouds and their top temperatures. For instance, aircraft soundings show liquid water occurrence (from the Johnson–William counter) and a virtual temperature inversion jump of about 7 K in coincidence with cloud top, and a strong specific humidity inversion (7 K decrease on equivalent potential temperature). From the set of all soundings, we kept only the ones indicating a presence of liquid water at the top of the boundary layer. The most limiting circumstance for the validation came from the frequent occurrence of cirrus clouds over the IZO area, as already mentioned.

Figure 8 shows the comparison between surface determination of the boundary layer CTT and our evaluation from satellite data. Despite the low number of possible comparisons (13 points in all), the results show extremely good correspondence: point-to-point variation is correct and the residual distance is only 0.5 K. A bias of 0.6 K is observed, far below the 2 K value found with the test for atmospheric absorption. These results confirm our hypothesis of neglecting possible spatial and temporal variations of the absorbing constituents of the free troposphere as compared with BL height variation. They also confirm a good selection of thick clouds. The quality of results is particularly satisfying given that the comparisons are often made at the border of high cloud sheets, so that undetected thin cirrus could have biased CTT evaluation.

To illustrate the quality of results in terms of spatial variation of the CTT, Fig. 9 places the different soundings done on 14 November on a trajectory along the

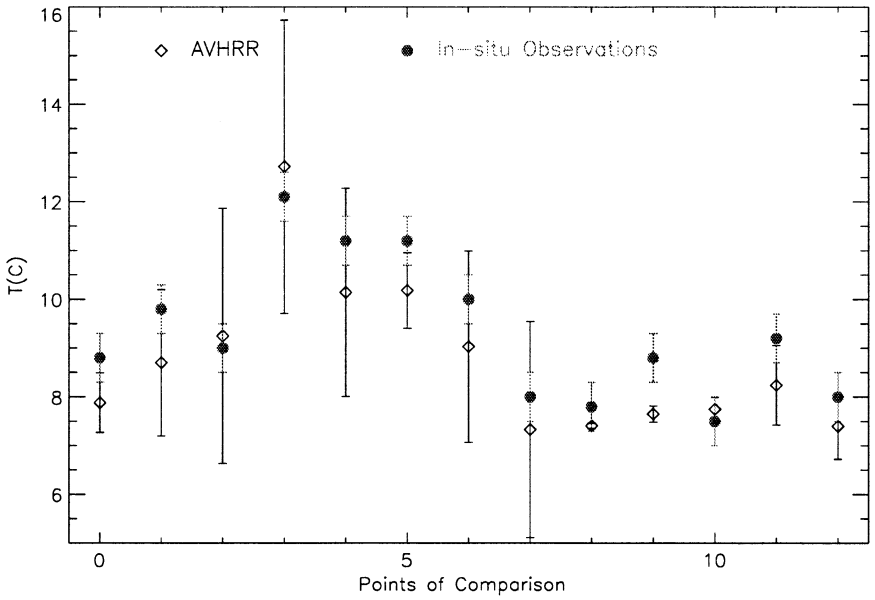

FIG. 8. Correspondence between satellite boundary layer CTT and surface measurements (radiosonde and aircraft sounding) between 10 and 17 Nov. Error bars for CTT retrieval are as explained in section 3b.

1727 UTC AVHRR CTT. The soundings, which are not included in the previous comparison because of overcast from higher clouds, appear to be in continuity with the retrieved temperature curve. The radio sounding from the ship, at about the same time, is particularly convincing.

5. Conclusions

We have built boundary layer CTT maps that cover large portions of a 3000×3000 km^2 region of the North Atlantic during an anticyclonic phase of the SEMAPHORE campaign. Based on this application, we propose a general method to determine maps of the BL cloud-top temperature from satellite observations. In the absence of mid- and high-level clouds, these determinations are made possible whenever thick BL clouds are present, as over extratropical regions. Such a documentation of the boundary layer can be used to situate a campaign IZO in its synoptic environment, as we did, and furthermore to explore regions hardly accessible to field experiments. It can be used to complement efficiently other types of BL cloud databases such as the one of Norris (1998), a climatological documentation of BL cloud structures from surface observations.

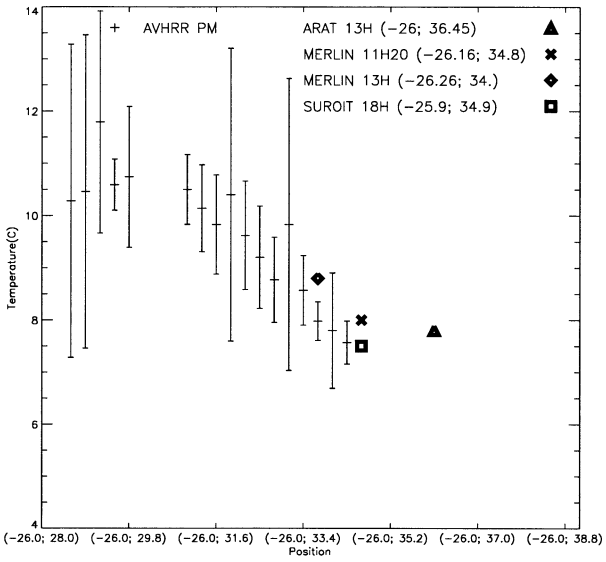

FIG. 9. CTT restitution from AVHRR at 1727 UTC 14 Nov along a trajectory between 28°N, 26°W and 39°N, 26°W, with close-by surface determinations from the ship *le Suroit* and two aircraft.

The temperature retrieval is based on a statistical cloud classification method, here applied to AVHRR images. Using the dynamic cluster method, sets of cloud classes are built, which allows for a good separation of BL clouds from upper cloud layers. Moreover, these classifications allow the distinction between regions of uniform Sc decks and regions in which the cloud cover is broken and more organized. Last, the documentation we propose of the boundary layer gathers two kinds of information: (i) CTT and associated error bars as a quantitative parameter and (ii) characterization of BL cloud structures in terms of uniform or broken decks. As compared with the ISCCP-DX database, the current method eliminates most of the pixels that are overcast by thin cirrus or are partially cloudy. For this reason, and the sampling method of the DX, our CTT maps exhibit a better spatial coherence. The results of the CTT retrieval method applied to the analysis of synoptic situations during the SEMAPHORE campaign were also success-

fully compared with surface-based measurements. This validation is important, in particular, because of the unfavorable zenith angles met.

Only two images per day were available during the period of study. Other periods could offer up to four high-resolution images. The launching of a new satellite generation (such as MSG[2]) should considerably increase the temporal coverage, giving access to the time evolution of the boundary layer. The temporal evolution of BL clouds may be combined with other information, like low-level cloud winds from tracking (as in Désalmand et al. 1999). This possibility to couple temporal analyses of the boundary layer over large regions is important to improve our understanding and modeling of BL processes.

Moreover, in theory, the method can be extended at nighttime (e.g., Olesen and Grass 1985) even if it may result in higher uncertainties, which should be included in the error-bar fields. Other radiometric channels can be useful in such cases [AVHRR (3.7 μm), MSG channels], and local IR variance should allow for thin cirrus rejection, which is not available in the ISCCP databases. Over continents, to the extent that the surface is not too glittering, the cloud classification method gives pertinent results (Sèze et al. 1999) and the CTT can be retrieved. In summary, with new satellites, we should be able to characterize the diurnal cycle of the boundary layer over extended continental surfaces.

We emphasize that CTT fields represent a documentation complementing the SST one and having a multiple interest: (i) providing a means to improve numerical weather prediction—as well as climatological reanalyses, (ii) representing a boundary layer global characterization, to analyze campaign situations at the synoptic scale, and (iii) allowing validation and testing development of large-scale and mesoscale models. Both CTT and uncertainty maps are important features of this application, because they combine information on (i) the existence of BL clouds at each gridpoint location, (ii) the inversion-layer temperature (or at least its spatial variation) as an important character of the state of the boundary layer, and (iii) the reliability of the CTT determination. Providing error-bar maps also allows one to keep the whole set of possible information on BL clouds, even in the neighborhood of cirrus sheets, and on broken clouds. This way, one can ensure a complete analysis of transitions from stratocumulus to cloud-free zones. Such a method is opposite to standard low-level-cloud CTT determination, in which margins of well-discriminated cloudy areas are removed from databases to avoid possible contamination (Rossow et al. 1985).

Mathieu et al. (2004) show how the database presented here may be used to evaluate models. Mathieu et al. (2002, manuscript submitted to *Mon. Wea. Rev.*) go further and propose a way to characterize physical processes of the boundary layer that explain the cloud transitions as observed in the region. In both cases, the precision and error bars of CTT maps are shown to be crucial.

Acknowledgments. The SEMAPHORE experiment has been supported by CNRS, Météo-France, SHOM, DRET, IFREMER, and ESA and was initiated by the program PATOM. The paper was written during the first author's stay at KNMI, funded by the European project CLIWA-NET. The authors thank Dr. Arnout Feijt for helpful discussions.

[2] Meteosat Second Generation.

REFERENCES

Agee, E. M., and K. E. Dowell, 1974: Observational studies of mesoscale cellular convection. *J. Appl. Meteor.,* **13,** 46–53.

Antoine, J. Y., M. Derrien, L. Harang, P. L. Borgne, H. L. Glau, and C. L. Goas, 1992: Errors at large satellite zenith angles on AVHRR derived sea surface temperatures. *Int. J. Remote Sens.,* **13,** 1797–1804.

Betts, A. K., P. Minnis, W. Ridgway, and D. F. Young, 1991: Integration of satellite and surface data using a radiative–convective oceanic boundary-layer model. *J. Appl. Meteor.,* **31,** 340–351.

Bretherton, C. S., and R. Pincus, 1995: Cloudiness and marine boundary layer dynamics in the ASTEX Lagrangian experiments. Part I: Synoptic setting and vertical structure. *J. Atmos. Sci.,* **52,** 2707–2723.

Buriez, J.-C., M. Doutriaux-Boucher, F. Parol, and N. G. Loeb, 2001: Angular variability of the liquid water cloud optical thickness retrieved from ADEOS–POLDER. *J. Atmos. Sci.,* **58,** 3007–3018.

Ciesielski, P. E., W. H. Schubert, and R. H. Johnson, 2001: Diurnal variability of the marine boundary layer during ASTEX. *J. Atmos. Sci.,* **58,** 2355–2376.

de Roode, S. R., and P. G. Duynkerke, 1997: Observed Lagrangian transition of stratocumulus into cumulus during ASTEX: Mean state and turbulence structure. *J. Atmos. Sci.,* **54,** 2157–2173.

Désalmand, F., A. Szantai, and M. Desbois, 1999: An attempt to retrieve low cloud motion winds over land in the African monsoon flow on Meteosat pictures. *Geophys. Res. Lett.,* **26,** 319–322.

Desbois, M., G. Sèze, and G. Szejwack, 1982: Automatic classification on Meteosat imagery: Application to high-level clouds. *J. Appl. Meteor.,* **21,** 401–413.

Eymard, L., and Coauthors, 1996: Study of the air–sea interactions at the mesoscale: The SEMAPHORE experiment. *Ann. Geophys.,* **14,** 986–1015.

Foot, J. S., 1988: Some observations of the optical properties of clouds. I: Stratocumulus. *Quart. J. Roy. Meteor. Soc.,* **114,** 129–144.

Giordani, H., and S. Planton, 2000: Modeling and analysis of ageostrophic circulation over the Azores oceanic front during the SEMAPHORE experiment. *Mon. Wea. Rev.,* **128,** 2270–2287.

Giraud, V., 1994: Caractéristiques des propriétés optiques et microphysiques des cirrus: Utilisation de l'imagerie satellite. Ph.D. thesis, Université des Sciences et Technologies de Lille, 202 pp.

Grossman, R. L., 1982: An analysis of vertical spectra obtained in the BOMEX fair-weather, trade-wind boundary layer. *Bound.-Layer Meteor.,* **23,** 323–357.

Harrison, E. F., P. Minnis, B. R. Barkstrom, and V. R. Ramanathan, 1991: Seasonal variation of cloud radiative forcing derived from the Earth Radiation Budget Experiment. *J. Geophys. Res.,* **95,** 18 687–18 703.

Krueger, S. K., G. T. McLean, and Q. Fu, 1995: Numerical simulation of the stratus-to-cumulus transition in the subtropical marine

boundary layer. Part I: Boundary layer structure. *J. Atmos. Sci.*, **52,** 2851–2868.
Lock, A. P., A. R. Brown, M. R. Bush, G. M. Martin, and R. N. B. Smith, 2000: A new boundary layer mixing scheme. Part I: Scheme description and single-column model tests. *Mon. Wea. Rev.*, **128,** 3187–3199.
Loeb, N. G., and J. A. Coakley, 1998: Inference of marine stratus cloud optical depths from satellite measurements: Does 1D theory apply? *J. Climate*, **11,** 216–233.
——, T. Varnai, and D. M. Winker, 1998: Influence of subpixel-scale cloud-top structure on reflectances from overcast stratiform cloud layers. *J. Atmos. Sci.*, **55,** 2960–2973.
Mathieu, A., A. Lahellec, and A. Weill, 2004: Evaluation of a numerical weather forecast model using boundary layer cloud-top temperature retrieved from AVHRR. *Mon. Wea. Rev.*, in press.
Minnis, P., P. W. Heck, D. F. Young., C. W. Fairall, and J. B. Snider, 1992: Stratocumulus cloud properties derived from simultaneous satellite and island-based instrumentation during FIRE. *J. Appl. Meteor.*, **31,** 317–339.
——, D. P. Garber, D. Young, R. Arduini, and Y. Takano, 1998: Parameterizations of reflectance and effective emittance for satellite remote sensing of cloud properties. *J. Atmos. Sci.*, **55,** 3313–3339.
Nicholls, S., and M. A. LeMone, 1980: The fair weather boundary layer in GATE: The relationship of subcloud fluxes and structure to the distribution and enhancement of cumulus clouds. *J. Atmos. Sci.*, **37,** 2051–2067.
Norris, J. A. M., 1998: Low cloud type over the ocean from surface observations. Part II: Geographical and seasonal variations. *J. Climate*, **11,** 383–403.
——, and C. A. Weaver, 2001: Improved techniques for evaluating GCM cloudiness applied to the NCAR CCM3. *J. Climate*, **14,** 2540–2550.
Olesen, F. S., and H. Grass, 1985: Cloud detection and classification over ocean at night with *NOAA-7*. *Int. J. Remote Sens.*, **6,** 1435–1447.
Platt, C. M. R., 1983: On the bispectral method for cloud parameter determination from satellite VISSR data: Separating broken cloud and semitransparent cloud. *J. Climate Appl. Meteor.*, **22,** 429–440.
Roozekrans, J. N., and G. J. Prangsma, 1986: Cloud clearing algorithms without AVHRR channel 3. *Abstracts, Second AVHRR Users Meeting*, Oxon, United Kingdom, Rutherford Appleton Laboratory.
Rossow, W. B., and Coauthors, 1985: ISCCP cloud algorithm intercomparison. *J. Climate Appl. Meteor.*, **24,** 877–903.
——, A. Walker, D. Beuschel, and M. Roiter, 1996: International Satellite Cloud Climatology Project (ISCCP) documentation of new cloud datasets. World Meteorological Organization Tech. Rep. WMO/TD 737, 115 pp.
Saunders, R. W., and K. T. Kriebel, 1986: An improved method for detecting clear sky and cloudy radiances from AVHRR data. *Int. J. Remote Sens.*, **7,** 867–886.
Sèze, G., and M. Desbois, 1987: A cloud cover analysis from satellite imagery using spatial and temporal characteristics of data. *J. Climate Appl. Meteor.*, **26,** 123–150.
——, and W. B. Rossow, 1991: Time-cumulated visible and infrared radiance histograms used as descriptors of surface and cloud variations. *Int. J. Remote Sens.*, **12,** 877–920.
——, and H. Pawlowska, 2001: Cloud cover analysis with *Meteosat-5* during INDOEX. *J. Geophys. Res.*, **106,** 28 415–28 426.
——, C. Vanbauce, J. C. Buriez, F. Parol, and P. Couvert, 1999: Cloud cover observed simultaneously from POLDER and Meteosat. *Phys. Chem. Earth*, **24B,** 921–926.
Stull, R. B., 1997: Parameterization of subgrid-scale tracer transport. CAS/JSC Working Group on Numerical Experimentation Rep. 26, Virginia Beach, VA, 148 pp.
——, 1998: Introduction to clear and cloudy boundary layers. *Clear and Cloudy Boundary Layers*, A. A. M. Holtslag and P. G. Duynkerke, Eds., Royal Netherland Academy of Arts and Science, 17–42.